communications physics

ARTICLE

https://doi.org/10.1038/s42005-023-01363-1 OPEN

Spiral spin cluster in the hyperkagome antiferromagnet Mn_3RhSi

Shin-ichi Shamoto[1,2,3,4✉], Hiroki Yamauchi[5], Kazuki Iida[1], Kazuhiko Ikeuchi[1], Amelia Elisabeth Hall[6], Yu-Sheng Chen[7], Min Kai Lee[2], Geetha Balakrishnan[6] & Lieh-Jeng Chang[2,4,8✉]

Local spin correlation orders emerge in a paramagnetic state, with notable examples such as the partial order, cooperative paramagnetism, and soliton spin liquid. The noncentrosymmetric intermetallic antiferromagnet Mn_3RhSi also exhibits the local spin correlation order in the paramagnetic state as magnetic short-range order in a wide temperature range. Here, we show that the local spin correlation order has a spiral structure by neutron scattering measurement of a Mn_3RhSi single crystal. The possible origins of the magnetic cluster formation are discussed in terms of the Lifshitz invariant and the Griffiths phase, and compared with the room-temperature skyrmion phase of $Co_7Zn_7Mn_6$ and non-Fermi liquid behavior of β-Mn.

[1] Research Center for Neutron Science and Technology, Comprehensive Research Organization for Science and Society (CROSS), Tokai, Ibaraki 319-1106, Japan. [2] Department of Physics, National Cheng Kung University, Tainan 701, Taiwan. [3] Advanced Science Research Center, Japan Atomic Energy Agency, 2-4 Shirakata, Tokai, Naka, Ibaraki 319-1195, Japan. [4] Institute of Materials Structure Science, High Energy Accelerator Research Organization (KEK), Tsukuba, Ibaraki 305-0801, Japan. [5] Materials Sciences Research Center, Japan Atomic Energy Agency, Tokai, Ibaraki 319-1195, Japan. [6] Department of Physics, University of Warwick, Coventry CV4 7AL, UK. [7] National Synchrotron Radiation Research Center, Hsinchu Science Park, Hsinchu 30076, Taiwan. [8] Institute of Physics, Academia Sinica, Taipei 115201, Taiwan. ✉email: s_shamoto@cross.or.jp; ljchang@ncku.edu.tw

Local spin correlation orders have been reported in a paramagnetic state[1–3]. Some typical examples are the partial order in MnSi[1, 4], the cooperative paramagnetism observed in $Tb_2Ti_2O_7$ below 50 K[2,5], and the soliton spin liquid of $Fe_{1-y}Te$[3]. The spin nematic state is also actively discussed as one of the possible examples[6]. These states may be categorized into the same class of the paramagnetic states with local spin correlation ordering. Similarly, a chiral spin liquid ground state is discovered by diffuse magnetic neutron scattering of $YBaCo_3FeO_7$ single crystal[7]. The local spin correlation orders form magnetic clusters, which can be observed by neutron scattering as magnetic short-range order (SRO). These unconventional phases in paramagnetic states cannot be described by the Landau–Ginzburg–Wilson (LGW) theory[8]. One of the origins can be violating the Lifshitz condition in the LGW theory of second-order magnetic transitions. The Lifshitz condition is known to be broken by noncentrosymmetric magnetic ordering with the Dzyaloshinskii–Moriya (DM) interaction[9–11] or the incommensurate magnetic order[3], where we may expect an unconventional order due to the inhomogeneous order parameter. These unconventional magnetic orders have been observed near critical points, which may be accompanied by local symmetry breaking. The conditions may be close to multicritical points[8]. Another possible origin is the Griffiths phase proposed in a ferromagnet with structural disorders[12]. The Griffiths phases are experimentally found in various magnets, such as colossal magnetoresistive oxides[13–16], 4*f*-type strong correlated systems[17,18], spin glass system[19], and frustrated antiferromagnet of $GdFe_{0.17}Sn_2$[20]. The Griffiths phase can be induced by small disorders under the competition of multiple ordered states[21]. It suggests that the frustrated spin system with high degeneracy of many spin configurations may become the Griffiths phase with small disorders. The Griffiths phase is experimentally defined as follows[20]. The Griffiths phase has magnetic clusters in the paramagnetic state, where the deviation from Curie-Weiss law becomes apparent at low magnetic fields below the Griffiths temperature, T_G. In the Griffiths phase, magnetization exhibits a relaxation behavior as a function of time.

Mn_3RhSi exhibits magnetic short-range order (SRO) up to 720 K far above the long-range order (LRO) magnetic transition temperature ($T_N = 190$ K), suggesting the magnetic cluster formation in the paramagnetic state. This might be evidence of a Griffiths phase in addition to the non-Curie-Weiss magnetic susceptibility above T_N[22]. On the other hand, Mn_3RhSi has a hyperkagome lattice of Mn spins with a noncentrosymmetric crystal structure[23]. This noncetrosymmetry with the DM interaction is relevant to the Lifshitz mechanism. The **Q**-position of the SRO centered at ~ 1.7 Å^{-1} does not coincide with any long-range magnetic Bragg peak positions. The **Q**-position is identical to the previously observed magnetic diffuse scattering position in β-Mn[24] and β-$Mn_{1-x}In_x$[25]. β-Mn is a well-known spin liquid candidate possessing a three-dimensional hyperkagome lattice with corner-sharing triangular Mn-spin units[23,24]. Non-Fermi-liquid (NFL) behavior is also identified in β-Mn, based on the exponent of the temperature dependence of the resistivity and the scaling of the dynamical spin susceptibility[26]. These unconventional physical properties can originate from the local spin correlation order observed as the magnetic SRO. Recently, a similar magnetic SRO is also observed in a skyrmion alloy of $Co_7Zn_7Mn_6$ with the same β-Mn crystal structure[27], suggesting a similar background among these magnetic states.

Here, we report a neutron scattering study of the magnetic SRO in a Mn_3RhSi crystal. The magnetic SRO comprises inelastic signals with a strong peak broadening in the **Q**-space. The observed inelastic signals are asymmetric in **Q**-space without the 4-fold symmetry of a cubic unit cell, suggesting the spiral spin structure.

Results and discussion

Nuclear and magnetic structures. The Mn_3RhSi crystal structure belongs to a noncentrosymmetric cubic space group of $P2_13$ (#198) with a lattice parameter of $a = 6.4665$ Å[22]. Mn atoms selectively occupy the 12-fold site (12*b*), similar to the Wyckoff 12*d* position of the β-Mn-type nuclear structure (Fig. 1a), whereas the Rh and Si atoms preferentially occupy two different 4-fold sites (4*a*) (Supplementary Note 1) derived by splitting the Wyckoff 8*c* position of β-Mn, as previously observed for this family[28–30]. The 12-fold site is the magnetic moment site of β-Mn

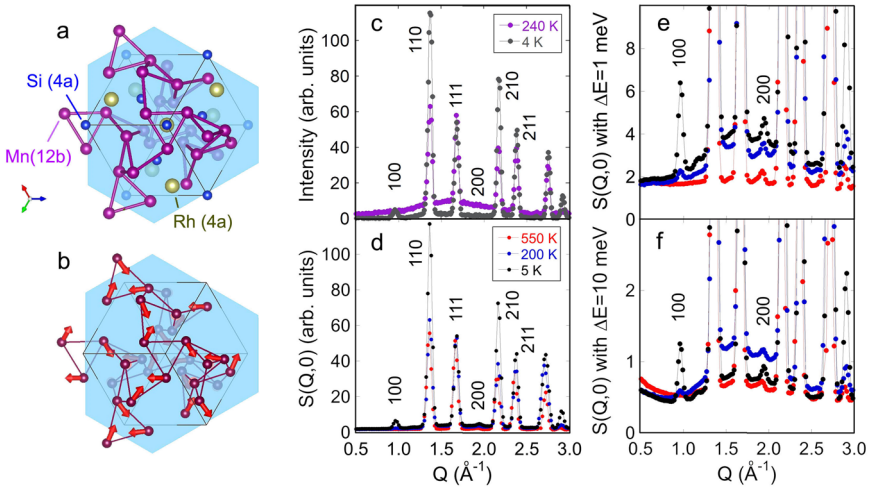

Fig. 1 Mn_3RhSi nuclear and magnetic structures and neutron elastic scattering patterns. a Mn_3RhSi crystal structure viewed along the[1,1,1] direction. A light blue (1,1,1) plane is inserted for clarity. **b** The 12*b* site of $P2_13$ is preferentially occupied by Mn magnetic moments. The nearest-neighbor (NN) bonds of $r = 2.69$ Å result in isolated Mn triangle clusters, whereas the second NN bonds of $r = 2.79$ Å bridge them, forming the hyperkagome lattice. **c** Neutron elastic scattering patterns of a polycrystal sample measured at the diffractometer WAND of HFIR[22]. The magnetic short-range order broad peak is observed around $Q = 1.7$ Å^{-1} at $T = 240$ K. **d** Neutron scattering patterns of a polycrystal sample measured at 4SEASONS with $E_i = 18$ meV. The intensity is integrated with the energy range from -1 to 1 meV at T = 5, 200, and 550 K. Long-range magnetic Bragg peaks such as 110 peak develop at $T = 5$ K. An Al cell Bragg peak is observed at Q = 2.7 Å^{-1}. **e** Enlarged neutron scattering patterns integrated with the energy range from -1 to 1 meV. **f** Enlarged neutron scattering patterns integrated with the energy range from -1 to 10 meV.

and forms a three-dimensional hyperkagome lattice as an ordered magnetic phase (Fig. 1b), whereas the Rh and Si atoms occupy the nonmagnetic sites in the β-Mn structure. According to the structural analysis of Supplementary Note 1, there were no site exchanges or defects in this crystal. This hyperkagome lattice can be viewed as a corner-sharing network of triangular units[23], where the Mn-Mn bond distance ranges from 2.64 to 2.84 Å. The small bond distance difference is introduced in the $P2_13$ space group. In the $Co_7Zn_7Mn_6$ case with the $P4_132$ space group, the Mn-Mn bond distance ranges from 2.67 to 2.69 Å. The bond difference becomes small, although nonmagnetic Zn atoms sit about two third of the 12-fold site (12*d*). The triangular units form a spiral chain along the[1,1,1] direction. The long-range magnetic structure is characterized by 120 degree-structure in the triangular unit (Supplementary Note 1).

Neutron scattering patterns. LRO magnetic Bragg peaks developed at 100, 110, and 210 below the Néel temperature T_N, as shown in Fig. 1c, d. The magnetic SRO is observed strongly around 111 above T_N in Fig. 1c, measured at a 2-axis diffractometer WAND of HFIR[22]. Here, we measured the same polycrystal sample on the inelastic neutron scattering (INS) spectrometer 4SEASONS of J-PARC MLF. The neutron scattering patterns near $E = 0$ meV are shown in Fig. 1d–f. Figure 1d shows the scattering patterns with integrated energy ranging from -1 to 1 meV, where the magnetic SRO is suppressed at all temperatures in comparison with Fig. 1c. The enlarged patterns show the highest SRO intensity at 5 K, which does not agree with the diffraction pattern in Fig. 1c. By extending the integration energy range up to 10 meV, the temperature dependence of the diffraction pattern was well reproduced as shown in Fig. 1f, suggesting the typical magnetic fluctuation energy of 10 meV. The energy integration is carried out on the positive energy side because of the instrumental asymmetric peak broadening on the negative energy side. We have not observed any incommensurate magnetic peaks reported in Co-doped β-Mn crystal[23].

Based on the typical magnetic fluctuation energy of 10 meV, the constant-energy maps integrated from 6 to 10 meV are sliced in Fig. 2 without any symmetry folding. Broad signals at $T = 200$ K are observed centered at {1,1,1} and {2,0,0}. The intensity anisotropy appears in the difference, for example, between (1,1,1) and (-1,1,1). As a result, the broad SRO signals have only 2-fold symmetry corresponding to the $P2_13$ space group. According to the crystal space group with a spiral structure, (h,k,l) is not equivalent to (-h,k,l), whereas (h,k,l) is equivalent to (-h,-k,-l) in the intensity.

Figure 3 shows constant-energy scans along [h,1,1], where the intensity is averaged based on the equivalence between [h,1,1] and [-h,-1,-1]. The intensity asymmetry between positive and negative side peaks is clearly shown at 6 and 200 K. The intensity anisotropy is consistent with a spiral spin cluster formation. The energy dependence of the dynamical spin susceptibility is plotted in Fig. 4a, b. The observed intensity anisotropy mostly disappears above 28 meV at 6 and 200 K.

The corresponding INS intensity maps were simulated using spherical magnetic cluster models (Fig. 5). The calculation details are described in Supplementary Note 2. The intensity asymmetry changes depending on the cluster size. The (1,1,1) intensity is stronger than that of (-1,1,1) in the 21 magnetic moments cluster (Fig. 5a, e, i, m, and q). The intensity difference almost disappears in the 24 magnetic moments cluster model (Fig. 5b, f, j, n, and r). Further increasing the cluster size to 27 (Fig. 5s), the observed intensity maps in Fig. 2 are well reproduced by the simulations in Fig. 5c, g, k, and o. For cluster size 42 (Fig. 5t), the simulated peak widths are narrower than the observed widths. The intensity

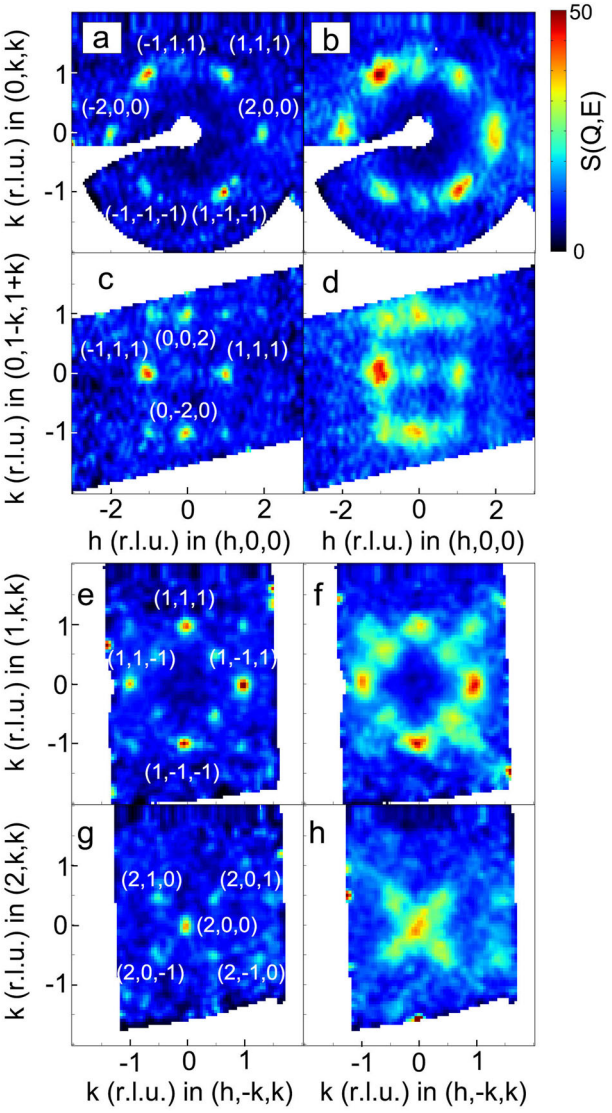

Fig. 2 Constant-energy maps integrated from $E = 6$ to 10 meV at $T = 6$ and 200 K. Constant-energy map of (h,0,0)-(0,k,k) plane measured with $E_i = 46$ meV at $T = 6$ K (**a**) and 200 K (**b**). Constant-energy map of (h,0,0)-(0,1-k,1+k) plane at $T = 6$ K (**c**) and 200 K (**d**). Constant-energy map in (1,-k,k)-(1,k,k) plane at $T = 6$ K (**e**) and 200 K (**f**). Constant-energy map of (2,-k,k)-(2,k,k) plane at $T = 6$ K (**g**) and 200 K (**h**). The color scale bar is the intensity of dynamical scattering factor S(Q,E) for a 200 K map, while the 6 K map intensity is multiplied twice. The intensity is integrated with the other reciprocal direction in 0.4 reciprocal lattice unit corresponding to 0.55 $Å^{-1}$ for **a**–**d** and 0.39 $Å^{-1}$ for **e**–**h**.

anisotropy change in Fig. 4 corresponds to the cluster size change. According to the scenario, the effective cluster size shrinks from 27 to 24 magnetic moments clusters with increasing the energy above 28 meV. It suggests high-frequency spin fluctuation removes the outer spins in the local spin correlation order.

Discussion

The magnetic spiral clusters in this metallic alloy are accompanied by itinerant electrons, usually described by the self-consistent renormalization theory of a nearly antiferromagnetic Fermi liquid[31]. According to the theory, the dynamical spin susceptibility χ"(E) increases linearly at low energies without a gap. We observed a hump structure around 15 meV at $T = 6$ K, as shown in Fig. 4a. The non-linear increase is inconsistent with the nearly antiferromagnetic Fermi liquid model[31]. In our previous

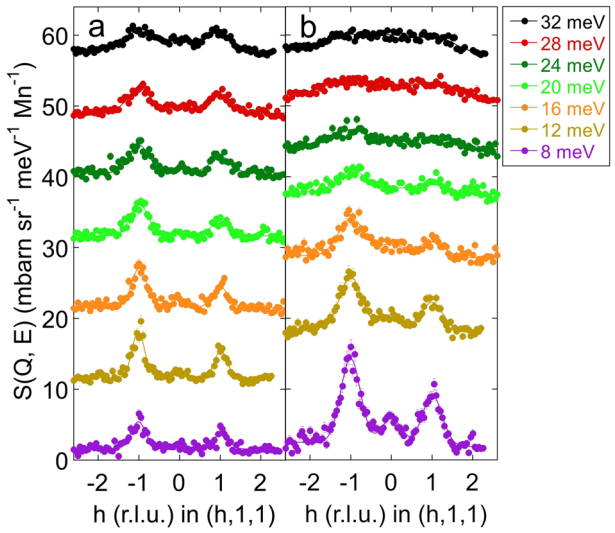

Fig. 3 Constant-energy scans of the dynamical structure factors S(Q, E) along [h,1,1]. S(Q, E) is measured with $E_i = 18$ ($E = 8$, 12 meV) and 46 meV ($E = 16$–32 meV) at $T = 6$ (**a**) and 200 K (**b**). The intensity is averaged based on the equivalence between [h,1,1] and [-h,-1,-1]. The intensity is integrated with the other two reciprocal directions in 0.22 Å^{-2} (0.4 ×0.4 reciprocal lattice unit^2). Each energy width is four meV.

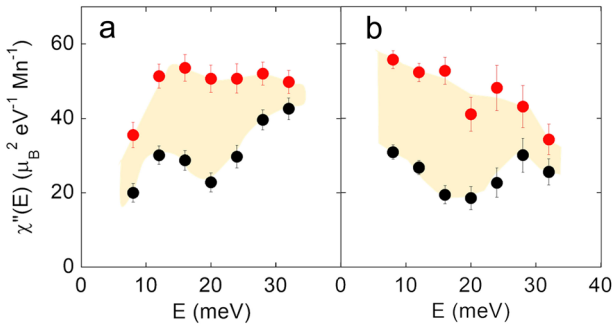

Fig. 4 Q-integrated dynamical spin susceptibility χ''(E) as a function of energy. The dynamical spin susceptibility χ''(E) at $T = 6$ K (**a**) and 200 K (**b**) is estimated from the constant-energy scans in Fig. 3, which is integrated along [h,1,1]. Red and black closed circles are measured at two **Q** positions (-1,1,1) and (1,1,1), respectively. The significant difference between them corresponds to a spiral spin dynamical structure factor. The errors (SD) are estimated based on the Gaussian fittings in the constant-energy scans of Fig. 3.

μSR measurement, the magnetic SRO is detected below 720 K as an initial asymmetry drop[22], where the spin excitation remains within the μSR energy window below 0.2 meV. The non-linear structure may be attributed to the present spiral spin cluster formation in the paramagnetic state. Note that a similar magnetic SRO is also observed in a skyrmion alloy of $Co_7Zn_7Mn_6$ with the same β-Mn crystal structure[27]. A skyrmion is one of the topological phases with a stable spin vortex. The similar magnetic SRO in the same β-Mn crystal structure suggests that the skyrmion alloy also has the spiral spin cluster.

Let us discuss the origin of the spiral spin cluster formation in the paramagnetic state. There can be two mechanisms. One is the Lifshitz invariant in a noncentrosymmetric magnet. The other is the Griffiths phase with quenched disorder. The former condition is satisfied because of the noncentrosymmetric lattice of Mn_3RhSi alloy with a DM interaction. The latter condition may not be satisfied fully because of no appreciable disorders in the crystal structure analysis. According to the structural study, the Mn_3RhSi crystal has few defects and no detectable elemental substitution in the lattice (Supplementary Note 1). The lack of disorder found in the structural analysis supports the Lifshitz mechanism. The relaxation behavior of the magnetization is not observed in Mn_3RhSi. In the magnetization measurement, however, Mn_3CoSi, another member of the same family is known often to exhibit hysteresis at low magnetic fields above T_N. This result suggests that Mn_3RhSi may also be close to the Griffiths phase. Another member of this family, Mn_3RhGe, is found to have two AF phases below the Néel temperature, suggesting the existence of competing orders. While the experimental evidence points to the former Lifshitz invariant being the most plausible mechanism, the Griffiths phase scenario with quenched disorder near the competing orders might also be a possible component contributing to the understanding of the variety of rich magnetic behavior in this Mn_3RhSi family of materials.

Conclusions

A spiral spin cluster is formed in a paramagnetic state of Mn_3RhSi above the Néel temperature T_N. In the temperature range between T_N and T_{SRO}, the temperature dependence of the magnetization does not obey the Curie-Weiss law[22]. This spiral spin cluster appears possibly due to the geometrical spin frustration in the hyperkagome lattice. This peculiar magnetic state can result from violating the Lifshitz condition due to the noncentrosymmetric lattice and the geometrical frustration of the hyperkagome lattice. A spin liquid candidate of β-Mn with non-Fermi-liquid behavior[24, 26] and a skyrmion alloy of $Co_7Zn_7Mn_6$[27] with noncentrosymmetric lattices commonly exhibit similar magnetic short-range orders. These magnetic short-range orders due to magnetic cluster formations in paramagnetic states may play an essential role in the realization of non-Fermi-liquid[26] and skyrmion states[27]. Primarily, the non-Fermi-liquid state may be easily understood by the cluster formation in a paramagnetic metallic state. This Mn_3RhSi alloy gives us an excellent platform to study these anomalous metallic states with the magnetic cluster formation over a wide temperature range, which will be attractive for the interdisciplinary study of the role of realizing these exotic states.

Methods

Sample preparation. A Mn_3RhSi crystal with a weight of 1.65 g was grown by the modified Bridgman method, starting from a high-purity Mn_3RhSi crystalline button placed in a commercial alumina crucible within an evacuated silica tube. The crystal orientations were checked by the X-ray Laue method. The crystal was wrapped in aluminum foil and then fixed on an aluminum plate by aluminum wires for the neutron experiment. The polycrystalline sample was synthesized by a conventional arc melting method in an argon atmosphere from stoichiometric amounts of powders of the constituent elements. The as-cast ingots were sealed in an evacuated quartz tube, annealed at 900 °C for 3 days and 800 °C for 1 week, and quenched in water. Crystal and magnetic structures were drawn by VESTA software[32].

Neutron scattering experiments. Both elastic and inelastic nonpolarized neutron scattering measurements were carried out on the chopper spectrometer 4SEASONS (BL01) with a multi-E_i option in J-PARC with a proton beam power of 500–600 kW[33,34]. The crystal was rotated by 210 degrees with a one-degree step for the rotation mode. The analyzed incident energies were 17.8 and 46.0 meV under a Fermi chopper frequency of 300 Hz. The energy resolutions at $E = 0$ for $E_i = 17.8$ and 46.0 meV are 0.67 and 2.48 meV, respectively. During the measurements, radial collimators were used. The data were analyzed by using 'Utsusemi' software[35]. The horizontal scattering plane was set by [h,0,0] and [0,k,k] with a vertical axis of [0,-k,k]. The observed

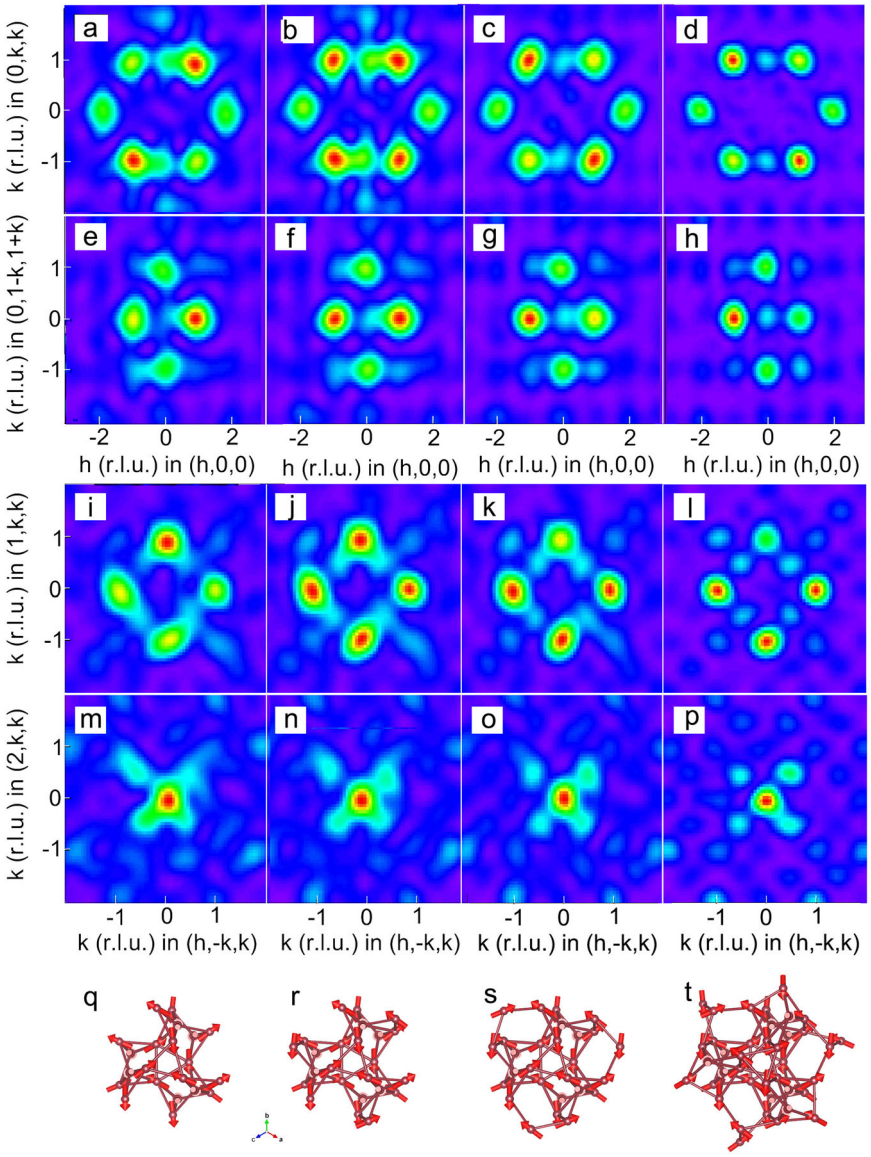

Fig. 5 Inelastic neutron scattering intensity maps of four magnetic cluster models. Simulated intensity maps (**a**–**d**, **e**–**h**, **i**–**l**, **m**–**p**) of four cluster models in (h, 0, 0)-(0, k, k), (h, 0, 0)-(0, 1-k, 1+k), (h, -k, k)-(1, k, k), (h, -k, -k)-(1, k, k), and (h, -k, -k)-(2, k, k) planes, respectively. The first raw maps (**a**, **e**, **l**, and **m**) are of 21 Mn magnetic moment (red arrows) cluster (**q**). The second raw maps (**b**, **f**, **j**, and **n**) are of 24 Mn magnetic moment cluster (**r**). The third raw maps (**c**, **g**, **k**, and **o**) are of 27 Mn magnetic moment cluster (**s**). The forth raw maps (**d**, **h**, **l**, and **p**) are of 42 Mn magnetic moment cluster (**t**). The magnetic cluster models are viewed along[1,1,1] direction of the original cubic lattice.

dynamic structure factors in Fig. 3 are estimated on an absolute scale (mbarn sr^{-1} meV^{-1} Mn^{-1}) by comparing the count rate with that from a plate of vanadium. The detector efficiency depending on E_f was also corrected. The imaginary part of the dynamical spin susceptibility is obtained by an equation for an isotropic paramagnet, including the Bose factor and the isotropic magnetic form factor for the Mn^{2+} 3*d* orbital.

Data availability

The datasets used and analyzed during the current study are available from the corresponding authors upon reasonable request.

Code availability

The code used during the current study is available from the corresponding authors upon reasonable request.

Received: 27 June 2023; Accepted: 28 August 2023;
Published online: 12 September 2023

References

1. Pfleiderer, C. et al. Partial order in the non-fermi-liquid phase of MnSi. *Nature* **427**, 227–231 (2004).
2. Gardner, J. S. et al. Cooperative paramagnetism in the geometrically frustrated pyrochlore antiferromagnet $Tb_2Ti_2O_7$. *Phys. Rev. Lett.* **82**, 1012–1015 (1999).
3. Materne, P. H. et al. Solitonic spin-liquid state due to the violation of the Lifshitz condition in $Fe_{1+y}Te$. *Phys. Rev. Lett.* **115**, 177203 (2015).
4. Uemura, Y. J. et al. Phase separation and suppression of critical dynamics at quantum phase transitions of MnSi and $(Sr_{1-x}Ca_x)RuO_3$. *Nat. Phys.* **3**, 29–35 (2007).
5. Villain, J. Insulating spin glasses. *Z. Phys. B* **33**, 31–42 (1979).
6. Fernandes, R. M., Chubukov, A. V. & Schmalian, J. What drives nematic order in iron-based superconductors? *Nat. Phys.* **10**, 97 (2014).

7. Schweika, W. et al. Chiral spin liquid ground state in $YBaCo_3FeO_7$. *Phys. Rev. X* **12**, 021029 (2022).
8. Belitz, D., Kirkpatrick, T. R. & Vojta, T. How generic scale invariance influences quantum and classical phase transitions. *Rev. Mod. Phys.* **77**, 579–632 (2005).
9. Dzyaloshinskii, I. E. Theory of helicoidal structures in antiferromagnets. I. nonmetals. *Sov. Phys. JETP* **19**, 960–971 (1964).
10. Tolédano, J. C. & Tolédano, P. *The Landau Theory of Phase Transitions* (World Scientific, Singapore, 1987).
11. Bogdanov, A. N. & Yablonskii, D. A. Thermodynamically stable "vortices" in magnetically ordered crystals. The mixed state of magnets. *Sov. Phys. JETP* **68**, 101–103 (1989).
12. Griffiths, R. B. Nonanalytic behavior above the critical point in a random Ising ferromagnet. *Phys. Rev. Lett.* **23**, 17 (1969).
13. Burgy, J., Moreo, A. & Dagotto, E. Relevance of cooperative lattice effects and stress fields in phase-separation theories for CMR manganites. *Phys. Rev. Lett.* **92**, 097202 (2004).
14. Salamon, M. B., Lin, P. & Chun, S. H. Colossal magnetoresistance is a Griffiths singularity. *Phys. Rev. Lett.* **88**, 197203 (2002).
15. Ibrahim, H. M., Yassin, O. A., de Chatel, P. F. & Bhatia, S. N. Evidence for the Griffiths phase in pure and Y-, Ca- and Cr-doped $LaSr_2Mn_2O_7$ manganites. *Solid State Commun.* **134**, 695 (2005).
16. Li, J. Q. & Yuan, S. L. Unusual magnetic and transport properties above the Curie temperature in $La_{2/3}Ca_{1/3}MnO_3$. *Solid State Commun.* **134**, 295 (2005).
17. Castro Neto, A. H., Castilla, G. & Jones, B. A. Non-fermi liquid behavior and Griffiths phase in *f*-electron compounds. *Phys. Rev. Lett.* **81**, 3531 (1998).
18. De Andrade, M. C. et al. Evidence for a common physical description of non-fermi-liquid behavior in chemically substituted f-electron systems. *Phys. Rev. Lett.* **81**, 5620 (1998).
19. Randeria, M., Sethna, J. P. & Palmer, R. G. Low-frequency relaxation in ising spin-glasses. *Phys. Rev. Lett.* **54**, 1321 (1985).
20. Ghosh, K., Mazumdar, C., Ranganathan, R. & Mukherjee, S. Griffiths behaviour in a frustrated antifferomagnetic intermetallic compound. *Sci. Rep.* **5**, 15801 (2015).
21. Burgy, J. et al. Colossal effects in transition metal oxides caused by intrinsic inhomogeneities. *Phys. Rev. Lett.* **87**, 277202 (2011).
22. Yamauchi, H. et al. High-temperature short-range order in Mn_3RhSi. *Commun. Mater.* **1**, 43 (2020).
23. Paddison, J. A. M. et al. Emergent frustration in Co-doped β-Mn. *Phys. Rev. Lett.* **110**, 267207 (2013).
24. Nakamura, H., Yoshimoto, K., Shiga, M., Nishi, M. & Kakurai, K. Strong antiferromagnetic spin fluctuations and the quantum spin-liquid state in geometrically frustrated β-Mn, and the transition to a spin-glass state caused by non-magnetic impurity. *J. Phys.: Condens. Matter* **9**, 4701–4728 (1997).
25. Stewart, J. R., Hillier, A. D., Hillier, J. M. & Cywinski, R. Structural and dynamical study of moment localization in $\beta\text{-}Mn_{1-x}In_x$. *Phys. Rev. B* **82**, 144439 (2010).
26. Stewart, J. R. et al. Non-Fermi-liquid behavior of electron-spin fluctuations in an elemental paramagnet. *Phys. Rev. Lett.* **89**, 186403 (2002).
27. Ukleev, V. et al. Frustration-driven magnetic fluctuations as the origin of the low-temperature skyrmion phase in $Co_7Zn_7Mn_6$. *npj Quantum Mater.* **6**, 40 (2021).
28. Eriksson, T., Bergqvist, L., Nordblad, P., Eriksson, O. & Andersson, Y. Structural and magnetic characterization of Mn_3IrGe and $Mn_3Ir(Si_{1-x}Ge_x)$: experiments and theory. *J. Solid State Chem.* **177**, 4058–4066 (2004).
29. Eriksson, T. et al. Crystal and magnetic structure of Mn_3IrSi. *Phys. Rev. B* **69**, 054422 (2004).
30. Eriksson, T., Bergqvist, L., Andersson, Y., Nordblad, P. & Eriksson, O. Magnetic properties of selected Mn-based transition metal compounds with β-Mn structure: experiments and theory. *Phys. Rev. B* **72**, 144427 (2005).
31. Moriya, T. *Spin Fluctuations in Itinerant Electron Magnetism* (Springer, Berlin 1985).
32. Momma, K. & Izumi, F. VESTA 3 for three-dimensional visualization of crystal, volumetric, and morphology data. *J. Appl. Crystallogr.* **44**, 1272–1276 (2011).
33. Kajimoto, R. et al. The fermi chopper spectrometer 4SEASONS at J-PARC. *J. Phys. Soc. Jpn.* **80**, SB025 (2011).
34. Nakamura, M. et al. First demonstration of novel method for inelastic neutron scattering measurement utilizing multiple incident energies. *J. Phys. Soc. Jpn.* **78**, 093002 (2009).
35. Inamura, Y., Nakatani, T., Suzuki, J. & Otomo, T. Development status of software "Utsusemi" for chopper spectrometers at MLF, J-PARC. *J. Phys. Soc. Jpn.* **82**, SA031 (2013).

Acknowledgements

This work at J-PARC was performed at 4SEASONS (BL01) under the proposals 2020A0052, 2021I0001, and 2021C0001. The neutron scattering experiment of WAND at ORNL was partly supported by the U.S.–Japan Cooperative Program on Neutron Scattering. A portion of this research was performed using resources at the ORNL HFIR and was sponsored by the Scientific User Facilities Division, Office of Basic Energy Sciences, U.S. Department of Energy. We would like to thank Profs. H. Kimura, T. Nakajima, Y. Yasui, Drs. R. Kajimoto, M. Nakamura, S. Onoda, and K. Kamazawa for valuable discussions and their help. This work was supported by Grants-in-Aid for Scientific Research (C) (No. 22K04678) from the Japan Society for the Promotion of Science. The work at the University of Warwick was funded by EPSRC, UK, through Grants EP/N032128/1 and EP/T005963/1. The crystal check was performed using an X-ray Laue camera at the MLF first experiment preparation room and a magnetic properties measurement system at the CROSS user laboratory II.

Author contributions

Mn_3RhSi crystals were grown by A.E.H. and G.B. with the help of Y.S.C., M.K.L. and L.-J.C. H.Y. synthesized the polycrystalline Mn_3RhSi sample. K.Ik., K.Ii. and S.S. carried out non-polarized INS. S.S. analyzed and calculated the INS patterns. H.Y. analyzed the nuclear and magnetic Bragg peaks. S.S. wrote this paper with input from the remaining authors. S.S. and L.-J.C. organized this research project. All authors have approved this manuscript.

Competing interests

The authors declare no competing interests.

Additional information

Supplementary information The online version contains supplementary material available at https://doi.org/10.1038/s42005-023-01363-1.

Correspondence and requests for materials should be addressed to Shin-ichi Shamoto or Lieh-Jeng Chang.

Peer review information *Communications Physics* thanks the anonymous reviewers for their contribution to the peer review of this work. A peer review file is available.

Reprints and permission information is available at http://www.nature.com/reprints

Publisher's note Springer Nature remains neutral with regard to jurisdictional claims in published maps and institutional affiliations.

Open Access This article is licensed under a Creative Commons Attribution 4.0 International License, which permits use, sharing, adaptation, distribution and reproduction in any medium or format, as long as you give appropriate credit to the original author(s) and the source, provide a link to the Creative Commons licence, and indicate if changes were made. The images or other third party material in this article are included in the article's Creative Commons licence, unless indicated otherwise in a credit line to the material. If material is not included in the article's Creative Commons licence and your intended use is not permitted by statutory regulation or exceeds the permitted use, you will need to obtain permission directly from the copyright holder. To view a copy of this licence, visit http://creativecommons.org/licenses/by/4.0/.

© The Author(s) 2023